Materials Advances

ROYAL SOCIETY OF CHEMISTRY

PAPER

View Article Online
View Journal | View Issue

Cite this: *Mater. Adv.*, 2025, 6, 6320

Graphene oxide/polyindole nanocomposite: a highly efficient multi-cyclic, stable and sustainable photocatalyst platform for wastewater remediation under visible light

Arisha Bi,[a] Sarfaraz Mahmood,[a] Nitika Garg,[b] Sahil Thakur,[c] Saif Ali Chaudhry,[a] Sarita Yadav,[d] Madhulika Gupta,[d] Mikhael Bechelany,[e] Jai Prakash *[c] and Zeba Haque *[a]

The present work focuses on visible light-driven photodegradation of anionic and cationic dye mixtures *via* metal-free and carbon-based multicyclic nanocomposites. In this context, graphene oxide (GO) has demonstrated tremendous potential in recent years as an excellent adsorbent and promising photocatalyst. Furthermore, conducting polymers (CPs) are emerging carbon-based materials with complementary photocatalytic properties. In this study, polyindole (PIn), a CP, was combined with GO to counter its major drawbacks such as hydrophilicity, chemical leaching, recyclability and difficulty in extraction. A series of GO/PIn composite photocatalysts, *i.e.* GO as *x*%GO/PIn (*x*% = 10, 15, 20 and 25), were synthesized *via* energy-economic *in situ* chemical oxidative polymerization. The GO/PIn nanocomposite showed improved structural, morphological and photoelectrochemical properties compared to bare materials. The composite exhibited enhanced visible light absorption with an optimized band gap of 2.59 eV and relatively low electron–hole recombination. GO/PIn exhibited 2.3-fold and 1.6-fold increases in photon-to-current efficiency compared to pure PIn and GO, respectively. This work provides an excellent sustainable photocatalyst platform (*i.e.* GO/PIn heterostructure nanocomposite) for wastewater remediation. The photodegradation of different mixtures of organic dyes that mimic wastewater conditions was performed under visible/solar-light conditions, which is rarely reported in the literature. The GO/PIn nanocomposite maintained high photostability and showed consistent photocatalytic efficiency over eight consecutive cycles, which prove its reusability. A detailed mechanistic scheme investigating the synergistic photocatalytic effect of GO and PIn in the GO/PIn nanocomposite is proposed, making it a promising and sustainable photocatalyst material for real-world applications.

Received 2nd May 2025,
Accepted 18th July 2025

DOI: 10.1039/d5ma00429b

rsc.li/materials-advances

1. Introduction

Water pollution is one of the major problems faced throughout the globe, primarily caused by the unregulated disposal of harmful organic chemicals such as dyes, pesticides, surfactants, fertilizers and other industrial effluents directly into waterways.[1] Dyes account for a major share among water pollutants as these synthetic dyes possess teratogenic, mutagenic, and carcinogenic tendencies and also increase the biological oxygen demand of the waterbodies. Thus, removal of synthetic dyes from waterbodies becomes a necessity as it can cause adverse health effects on flora and fauna.[2,3] A variety of physical and chemical methods such as adsorption, membrane filtration, coagulation–flocculation and catalytic degradation are employed for the removal of dyes from waterbodies.[4,5] Photocatalysis by far is considered the best method of wastewater treatment as it counters the backlogs of other methods owing to its irreversible nature, fast reaction time and relatively high efficiency in terms of cost and energy.[6,7] The most prominent photocatalysts used are metal oxide-based semiconductor materials such as TiO_2, SnO_2, WO_3, and ZnO and their composites, which have a major drawback of having a narrow photoactive region due to their large band gap and rapid recombination rate of photoinduced electrons.[8–10] Weak adsorption, heavy metal toxicity and

[a] *Department of Chemistry, Jamia Millia Islamia University, New Delhi, 110025, India. E-mail: zeba@jmi.ac.in*
[b] *Department of Chemistry, Indian Institute of Technology Delhi, New Delhi, 110016, India*
[c] *Department of Chemistry, National Institute of Technology Hamirpur, Hamirpur, HP 177005, India. E-mail: jaip@nith.ac.in*
[d] *Department of Chemistry and Chemical Biology, Indian Institute of Technology (Indian School of Mines), Dhanbad, Jharkhand, 826004, India*
[e] *Institut Européen des Membranes, IEM, UMR-5635, University Montpellier, ENSCM, CNRS, Place Eugene Bataillon, 34095 Montpellier, France*

agglomeration further add to the disadvantages of metal oxide-based photocatalysts.[11–13]

Metal-free two-dimensional (2D) carbon compounds such as graphene and chemically produced graphene oxide (GO) have recently gained popularity as cost-effective, non-toxic substitutes for the metal oxide-based photocatalyst owing to their tendency to act as excellent sole adsorbents and efficient photocatalysts.[14,15] However, the use of GO alone is limited by certain drawbacks such as structural instability in a harsh chemical environment, considerable electron–hole recombination rate, and difficult post-catalytic extraction due to hydrophilicity.[16] A material with such complementing properties can be incorporated within the GO matrix in order to further strengthen its structural stability, recyclability, and photocatalytic activity. Conducting polymers (CPs) are an emerging class of materials, which can add exceptional physicochemical properties to the primary photocatalysts that had been reported to enhance chemical stability and surface-active catalysis due to their hydrophobic nature.[17] For example, Hanafi *et al.* prepared a PANI/GO composite and reported excellent results for the photodegradation of 2-chlorophenol.[18] Gunawardana *et al.* synthesized a GO/PPy composite and studied the removal of cationic rhodamine B (RhB) and anionic methyl orange (MO).[19] Recently, PIn has gained much popularity in the field of sustainable catalysis due to its remarkable conductivity, cyclic and thermal stability and ability to act as electron reservoirs. It solely possesses the properties of both the PPy and poly(*para* phenylene), where it effectively combines the excellent environmental stability, high electrical conductivity, and long cycling stability of PPy with the superior thermal stability of poly(*para*-phenylene).[20]

In this study, the above-discussed synergistic relationship was obtained by incorporating a CP, polyindole (Pln), within the GO matrix to obtain a composite heterostructure (GO/Pln).[21] The combination of PIn with GO and other similar materials has been developed and tested for applications such as sensing and energy storage where the nanohybrid showed promising results. However, its use as a photocatalyst remains relatively unexplored till date.[22,23] Pln serves the role of secondary photocatalyst owing to its optoelectronic properties and suitable band structure.[24] For example, Megha *et al.* investigated the photodegradation of Congo red dye using Fe_2O_3–PIn composites and achieved 60% degradation by pure Pln itself, demonstrating its potential as a photocatalyst.[25] In another study, Singha *et al.* prepared a ternary hybrid microsphere photocatalyst with mercaptoacetate-functionalized PIn (PIn/MAA), $Ni(OH)_2$ nanoflowers and Ag. This ternary hybrid was utilized for the photocatalytic degradation of tetracycline, yielding excellent results. The presence of PIn in the microsphere increased light absorption and also reduced the recombination of photoinduced electron–hole pairs, thereby enhancing the overall photocatalytic activity.[26] However, to the best of our knowledge, the composite based solely on GO and PIn had never been employed for photocatalytic applications. This article deals with the synthesis, characterizations and detailed investigations of the photocatalytic performance of sustainable GO/Pln nanocomposites for the visible light driven-photodegradation of multiple dyes and their mixtures. The mixtures of dyes were selected as target pollutants to simulate real wastewater conditions. Only a few studies on the photocatalytic degradation of dye mixtures are available till date (Table S1), with a lack of specific data addressing the degradation of cationic and anionic dye mixtures separately. The GO/PIn nanocomposites were synthesized by varying the GO content in the PIn matrix (*i.e.* 10, 15, 20 and 25 wt%). Thus, the GO/PIn composite was ascertained to exhibit the complementing properties of both the GO and Pln, which could harness the fullest potential of solar radiation and demonstrate excellent multicyclic photocatalytic performance. This research article aims to broaden the potential application of GO/PIn nanocomposites for the photodegradation of a sample imitating real wastewater conditions with detailed morphological, analytical and optoelectronic analyses.

2. Experimental

2.1. Materials

Indole (analytical grade) was purchased from CDH Fine Chemicals, New Delhi, India. Ferric chloride ($FeCl_3$, 98%), $KMnO_4$, and $K_2Cr_2O_7$ were obtained from Sisco Research Laboratories (SRL), New Delhi, India. Graphite flakes (98% extra pure) were sourced from Loba Chemie Pvt. Ltd, Mumbai, India. H_2SO_4 (97%, Rankem) was purchased from Avantor Performance Materials India Ltd and H_2O_2 (30%) was purchased from Merck Life Science Pvt. Ltd. Hydrochloric acid (HCl, 38% wt/wt, analytical grade) and ethanol (analytical grade) were obtained from Qualigens. Ethylenediaminetetraacetic acid (EDTA), *p*-benzoquinone (BQ) and isopropyl alcohol (IPA) were supplied by SRL, New Delhi, India. Double-distilled water was used to prepare the aqueous solutions, and dilute HCl and NaOH solutions were used to adjust the pH.

2.2. GO synthesis

GO was synthesized using improved Hummers' method, as reported previously.[27] In brief, 97 ml of H_2SO_4 was slowly added to 5 g of graphite flakes under stirring in an ice bath at 10 °C. To this solution, 3 g of $K_2Cr_2O_7$ and 3 g of $KMnO_4$ were added and stirred for 2.5 h. Furthermore, 3 g of $KMnO_4$ was added to the reaction mixture followed by stirring at 40 °C for 5 hours. 250 ml of H_2O was then added to the reaction mixture while increasing the temperature up to 100 °C. After hydrolysis, 6.5 ml of H_2O_2 was added to the reaction mixture to quench the reaction and remove the excess oxidizing agents.

2.3. PIn synthesis

PIn was synthesized by employing a simple *in situ* polymerization technique.[22] The solution of $FeCl_3$ was prepared by adding 10.66 g to 80 ml of 0.1 M HCl, which was used as a solvent. Then, 3 g of indole monomer was separately dissolved in 10 ml of ethanol. The $FeCl_3$ solution was then kept under stirring and indole solution was added dropwise to it. The resulting mixture was constantly stirred at room temperature for 24 hours. The obtained precipitate was then filtered and washed with double-distilled water until the yellowish color of the filtrate disappeared. The resulting precipitate was then dried at 70 °C for 24 hours to obtain PIn.

2.4. Composite preparation *via in situ* chemical oxidative polymerization:

Composites were synthesized using the *in situ* chemical oxidative polymerization technique, as shown in Fig. 1. Initially, GO in different wt% (ranging from 10 to 25 wt%) was sonicated in 100 ml of 0.1 M HCl, for about 30 minutes to separate the GO layers. A sonicated solution was then cooled down to room temperature by stirring to eliminate extra heat. Meanwhile, the solution of $FeCl_3$ was prepared by dissolving 10.66 g in 80 ml of 0.1 M HCl. Both the solutions were mixed and kept under stirring for 10 minutes. Then, 3 g of indole monomer was dissolved in 10 ml of ethanol and dropped gradually into the solution under stirring. The mixture was further stirred at room temperature for 24 hours. The precipitate obtained was washed in a similar way as done for PIn. Post synthesis, the composites were named depending on the wt% of GO added into the PIn matrix as 10%GO/PIn, 15%GO/PIn, 20%GO/PIn, and 25%GO/PIn.

2.5. Methods of characterizations

Powder X-ray diffraction (PXRD) was used to examine the structural characteristics using an X-ray diffractometer with Cu Kα (λ = 0.15406 nm) radiation in the 2θ = 8°–90° range. For the determination of functional groups in GO, PIn and all the composites, Fourier transform infrared (FTIR) spectroscopy was performed using a PerkinElmer spectrometer in the KBr mode. Field emission scanning electron microscopy (FESEM-EDAX) was performed using a high-resolution JIB-PS500i FIB-SEM microscope at an accelerating voltage of 10 kV and a working distance of 10 mm for studying the morphology and elemental composition. For the accurate elemental compositions, surface functionalities and chemical bonding state, X-ray photoelectron spectroscopy (XPS) was performed using a PHI III 5000 Versa probe scanning XPS microprobe. Brunauer–Emmett–Teller (BET) analyses were performed using a BELSORP-maxll (BELSORP-series) instrument in a N_2 atmosphere to determine the porosity and the surface area of the samples. The zeta potential was recorded using a Malvern Zetasizer Nano ZSP (5600) with water as the dispersant. For studying the optical properties of the samples, UV-visible spectroscopy was performed using a Perkin Almer UV-2100 UV-vis spectrometer in the range of 200 to 800 nm and the band gap was further calculated using the Tauc plots. Photoluminescence (PL) spectra were recorded using a WITec Alpha-300 laser-based photoluminescence spectrophotometer, at an excitation wavelength of 325 nm. Electron spin resonance (ESR) measurements were carried out in the dark and under visible light irradiation for 10 min using a JOEL JES-X320 instrument with 1 mg mL^{-1} photocatalyst and 50 mM DMPO in methanol and aqueous media. Photoelectrochemical measurements were carried out in a Teflon cell using an AutoLab PGSTAT204 workstation equipped with a 300 W Xe arc lamp. The lamp provided illumination under AM 1.5 G simulated solar conditions with a power density of 100 mW cm^{-2}. For the fabrication of photoelectrodes, 2 mg of the catalyst was dispersed in 200 μL of cyclohexane and sonicated to form a uniform ink. This ink was then drop-cast onto an FTO substrate and allowed to air dry. The working electrode was the catalyst-coated FTO, while an Ag/AgCl (3 M KCl) electrode served as the reference and a Pt wire functioned as the counter electrode. A 0.1 M KOH solution was used as an electrolyte in this study. Linear sweep voltammetry (LSV) measurements were performed over a potential range of 0 to 1 V *vs.* Ag/AgCl (3 M KCl) under both dark and illuminated conditions, at a scan rate of 50 mV s^{-1}. Electrochemical impedance spectroscopy (EIS) studies were conducted in the dark as

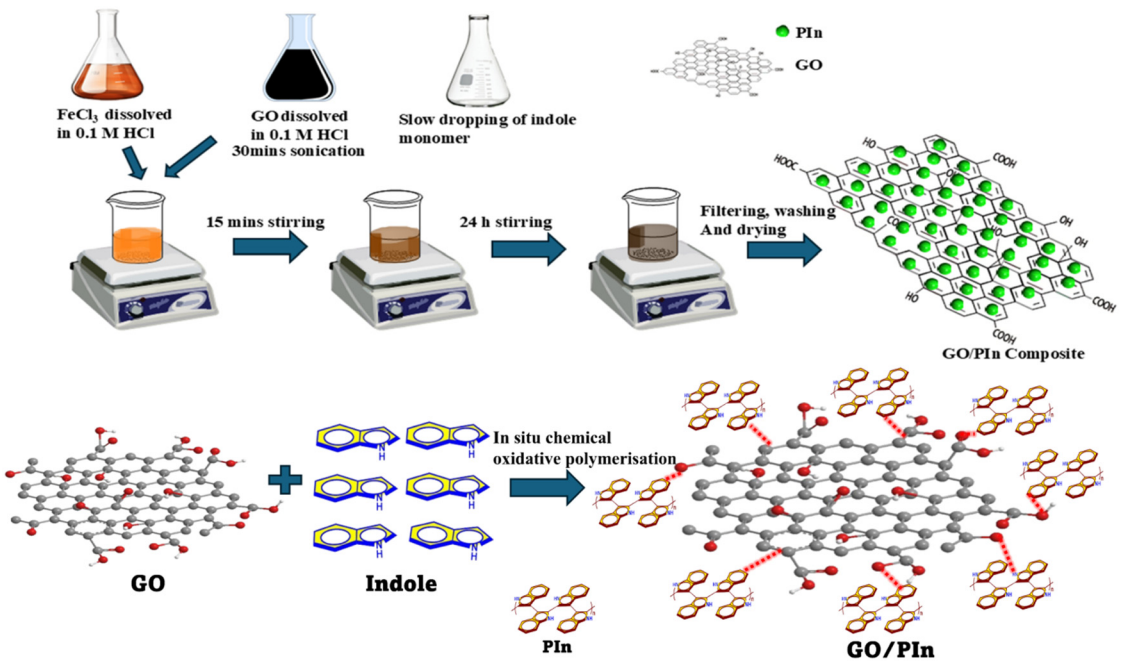

Fig. 1 Schematic representation of the GO/PIn composite synthesis *via in situ* chemical oxidative polymerization.

well as in the presence of light at an applied potential of 1.8 V *vs.* RHE, using an AC voltage across a frequency range of 0.1 to 10^5 Hz. Mott–Schottky studies were conducted in the dark at a frequency of 1000 Hz. The applied bias photon-to-current efficiency (ABPE) of the synthesized catalysts was determined at 1.2 V *vs.* RHE. Additionally, chronoamperometric on/off measurements were carried out to determine the transient photocurrent responses, enabling the evaluation of both photostability and photoresponsivity.

2.6. Photocatalytic experimental setup

The photocatalytic efficiency of the synthesized catalysts was initially evaluated for the degradation of acridine orange (AO) and eosin yellow (EY) dyes to determine the best catalyst composition. Following that, tests were conducted on fifteen different dyes, namely, AO, EY, victoria blue (VB), basic fuchsin (FB), alizarin red (AR), bismarck brown (BB), auramine (Au), Coomassie brilliant blue R (CBBR), bromocresol green (BCG), congo red (CR), methyl violet (MV), methylene blue (MB), rhodamine B (RhB), toluidine blue (TB), and crystal violet (CV). Further studies were conducted by preparing cationic and anionic dye mixtures separately, and photoreaction parameters such as catalytic dosage, initial dye concentration and pH were optimized to obtain the optimum photocatalytic efficiency. The anionic dye mixture contains AR, EY, CBBR and BCG, whereas the cationic dye mixture consists of AO, BB, FB and VB. Initially, the stock solution (100 ppm) of each mentioned dye was prepared to be used in further reactions. For single dye degradation, 40 ml (10 ppm) solution of target dye sample was prepared and 10 mg of the catalyst was added. Dye mixtures were prepared by mixing 10 ml solution of each dye present in the mixture, each in definite concentrations. Further, required catalyst dosage was added and kept in the dark for 30 minutes for the adsorption–desorption equilibrium to be attained. The sample solution was then kept under visible light irradiation using a 400 W white LED lamp, keeping the distance between the light and the sample solution to be around 25 cm. Then 3 ml aliquots were collected at specific time intervals for the duration of 120 minutes. After the optimization of reaction parameters, a final degradation reaction was set up for 300 minutes for both the cationic and anionic mixtures, separately. The changes in the concentration of the aliquots taken were analyzed by reading the absorption spectra using a Perkin Almer UV-2100 UV-vis spectrometer. For the final degradation reactions, full-range spectra from 400 to 700 nm were recorded, while the rest of the studies were conducted by recording the absorption spectra at specific maximum wavelength (λ_{max}) values. For evaluating the percentage degradation (C%), the following equation is used:

$$\%C_{deg} = \frac{C_0 - C_t}{C_0} \times 100 \quad (1)$$

2.6.1. Scavenger studies. To deduce the photocatalytic reaction mechanism, scavenger studies were conducted to examine the effect of reactive radical species taking part in the photodegradation reaction. Benzoquinone (BQ, 1 mM), isopropyl alcohol (IPA : H_2O, 2 : 18) and ethylenediaminetetraacetic acid (EDTA, 10 mM) were used as scavengers for superoxide ($^{\bullet}O_2^-$), hydroxyl ($^{\bullet}OH$) radicals and holes (h^+), respectively. Then, 1 ml of each scavenger solution was added to the photocatalytic reaction mixture to capture holes h^+, $^{\bullet}O_2^-$ and $^{\bullet}OH$.

3. Results and discussion

3.1. Powder X-ray diffraction

The powder X-ray diffraction (PXRD) analysis for GO, PIn and all GO/PIn composites was performed within the 2θ range of 8°–90°. The diffraction patterns confirm the presence of the expected phases, indicating the successful synthesis of the materials, as shown in Fig. 2(a). The most crystalline and characteristic peaks for GO were observed at 2θ = 10.31° (001), 26.15° (002) and 42.5° (100). The peak present at 2θ = 26.15° (002) with a d spacing of 3.40 Å corresponds to a graphitic moiety.[28] The GO formation was validated by the peak at 10.31° with the reflection plane (001) and d spacing of 8.57 Å, emphasizing the successful oxidation between the graphitic layers.[29] Furthermore, the peak present at 2θ = 42.5° (100) was observed due to the disordered arrangement of the carbon materials. PIn displays a wide amorphous peak at 2θ = 19.90° owing to the polymerization of indole. A relatively sharper peak at 2θ = 26.8° denotes the semi-crystalline

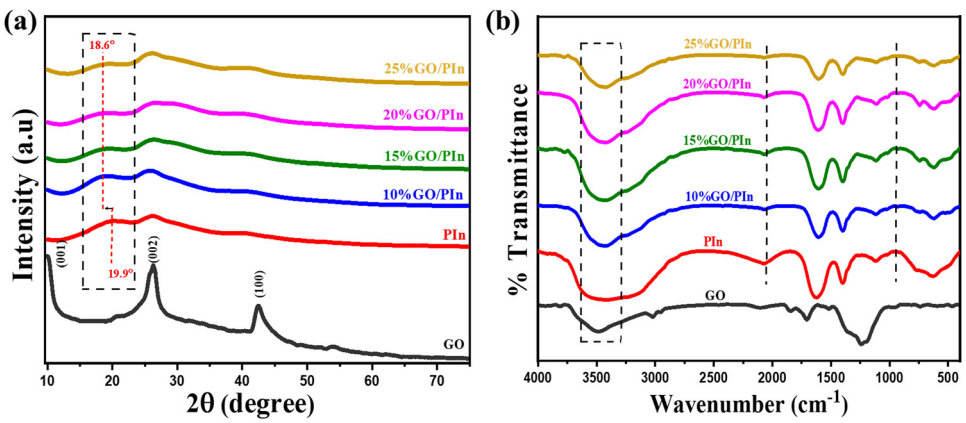

Fig. 2 (a) PXRD pattern and (b) FTIR spectra of the GO, PIn and GO/PIn composites.

nature of the polymer backbone.[30] The interchain spacings (S) between the polymer chains in PIn were calculated using eqn (2) and found to be 4.218 Å, which is comparable to that obtained by Gopika *et al.*[24]

$$S = \frac{5\lambda}{8\sin\theta} \quad (2)$$

where λ represents the X-ray wavelength (1.54 Å) and θ is the Bragg diffraction angle of the peak with highest intensity. The S value gives an idea about the conductivity of the respective polymer by virtue of the chemical nature and arrangement between the chains.[24] The PXRD pattern of all the four GO/PIn composites showed a slight shifting in the 2θ from 19.90° to a lower diffraction angle of 18.6°, which corresponds to the distortion of the GO layers by PIn insertion, hence an increase in the distance between the two consecutive GO sheets.[31] The successful interactions between GO and the polymer matrix can be confirmed by the increase in the intensity at 26.8°and the decrease in the intensity at 19.9° peaks, as the amount of GO into the PIn increases.[24]

3.2. FTIR spectroscopy

The FTIR spectroscopy for GO, PIn and all the composites was performed between the range of 4000–400 cm^{-1} in the solid (KBr pellets) mode, and the spectra are given in Fig. 2(b). For pure GO, the two intense broad bands present at around 3500 cm^{-1} and 1236 cm^{-1} correspond to the –O–H stretching and –C–O vibration of the hydroxyl group (–OH), respectively.[32] The peak at 1702 cm^{-1} was due to the C═O stretching of the carbonyl and carboxyl groups. The weak bands at 3015 cm^{-1} and 2946 cm^{-1} illustrate the asymmetric and symmetric stretching of CH_2. Furthermore, the less intense bands at 1505 cm^{-1} and 1351 cm^{-1} were ascribed to the skeletal C═C vibration and tertiary –C–OH groups, respectively.[33,34] In the PIn spectra, a broad band ranging from 3000 to 3600 cm^{-1} corresponds to the –N–H stretching vibration. The peaks observed at 1625, 1405, 1109 and ∼736 cm^{-1} correspond to the C═C stretching vibration of the aromatic ring in indole, benzene ring stretching, –C–N bond vibration and –C–H stretching vibrations, respectively.[35] The spectra of all the GO/PIn composites exhibited similar peaks as PIn with a slight shift in –NH and –CH stretching peaks to the lower wavenumbers, with the –CH out-of-plane deformation peak being more prominent in composites. The presence of GO in PIn makes the growth restricted and modes of vibration become confined, resulting in this shift in the wavenumber.[22,36] Phasukom *et al.* observed a similar shift in the wavenumber upon forming a composite of PIn with graphene-based materials including GO, which can be attributed to the π–π interactions arising from the overlap of the π-orbitals of the non-planar aromatic rings in both GO and PIn.[37] A trend of gradual decrease in the peak intensities of the composites from 10%GO/PIn to 25%GO/PIn was also observed relative to the pure PIn. This decrement in intensities was a result of PIn incorporation into the GO layers which led to the interaction of GO with PIn. The shift in wavenumber and decrease in peak intensity confirm the successful formation of GO/PIn composites.

3.3. UV-vis spectroscopy

The optical properties of GO, PIn and the composites were determined by UV-vis spectroscopy at room temperature, as shown in Fig. 3(a). The absorption spectrum of GO was obtained at 253 nm arising due to π–π* transition, whereas the n–π* transition causes a slight hump at about 305 nm.[34] PIn displays an absorption spectrum in the range of 210–400 nm. The high-intensity peak present at 214 corresponds to π–π* transitions in the benzenoid ring. The peaks present at ∼253, 274, 307 and 347 nm are attributed to π–π*transitions obtained because of an extended conjugation in the PIn matrix.[38,39] The less intense peaks between 348 and 398 nm are due to n–π* and the polaronic transitions.[40,41] The composites displayed a similar absorption spectrum as PIn, but with a significantly higher intensity. It is evident from the spectra that the light absorption capacity has increased substantially after the composite formation due to an increased surface area.[24,42] The highest absorption capacity was observed for the 15%GO/PIn composite with the decrease in the absorbance on further increasing the GO concentration. The phenomenon of red shift was observed in the composites, where the peak present at 214 nm in PIn shifted to longer wavelengths for all the composites with the highest shift observed in 15%GO/PIn to 223 nm.[43,44] It is clear from the spectra that synergistic interactions between GO and PIn have significantly increased the light absorption capacity of the composites, reflecting the role of GO in the enhancement of optical properties of PIn by increasing the surface area at nanoscale.[45]

3.3.1. Optical bandgap energy. The bandgap energy of all the synthesized materials was calculated by plotting the graph between $(\alpha h\nu)^2$ and the energy of photon ($h\nu$) using the following Tauc equation (eqn (3)):[34]

$$\alpha h\nu = A\,(h\nu - E_g)^{n/2} \quad (3)$$

where α, h, ν and E_g represent the absorption coefficient, Planck's constant, light frequency and band gap energy, respectively. The lowest band gap was obtained for the 15%GO/PIn composite (Fig. 3(b)), which might be attributed to its high visible light activity compared to the other composites. The band gap of the 15%GO/PIn composite was also confirmed by the UV-DRS, and is given in Fig. S1 and S2. The band gap values for all the materials are listed in Table 1.

The Urbach energy (Urbach edge or band tail) denoted by E_u, which was used for the determination of band edge disorderness of the semiconducting samples, was calculated as shown in Fig. 3(c). It is used to analyze the crystallinity of the material after doping where E_u is inversely proportional to the crystallinity.[46] The equation given by Franz Urbach for the determination of E_u is as follows:[47]

$$\alpha = \alpha_0 \exp\left(\frac{h\nu}{E_u}\right) \quad (4)$$

The absorption coefficient (α) depends on the energy of the photon ($h\nu$) exponentially, for the amorphous and crystalline materials near their band edges. The E_u value can be calculated graphically from the plot of $\ln\alpha$ *vs.* $h\nu$, by determining the

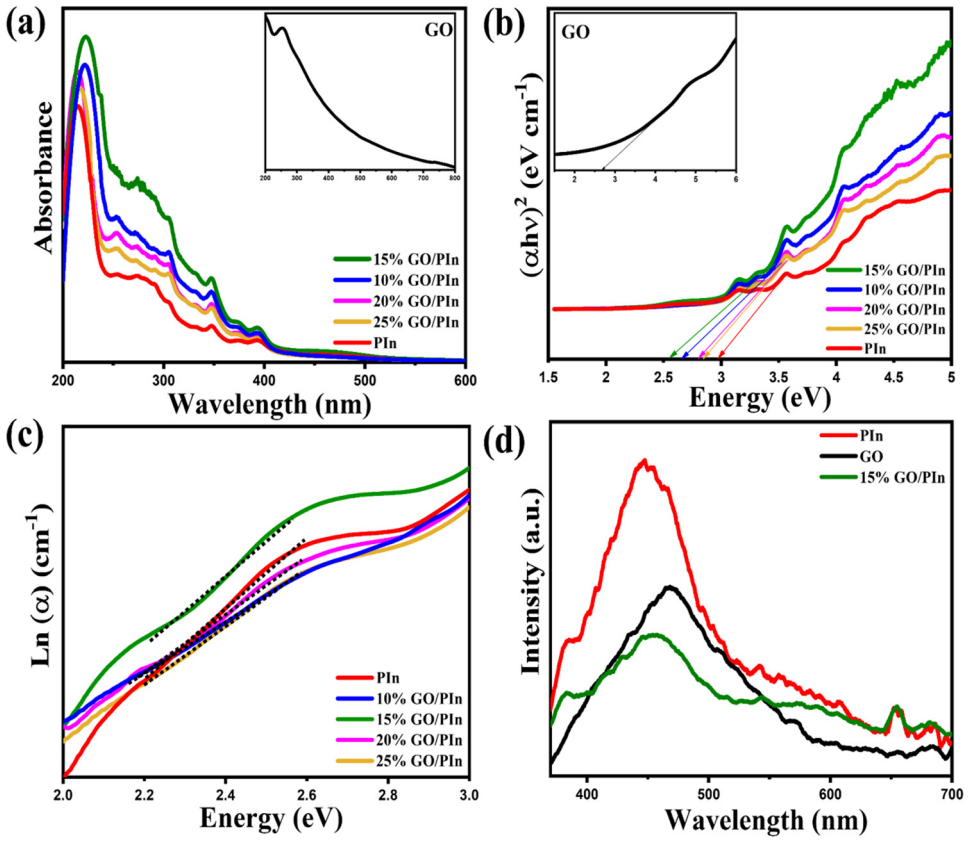

Fig. 3 (a) UV-visible spectra, (b) Tauc plots for PIn and composites (insets: GO absorbance spectra and Tauc plot, respectively), (c) Urbach energy plots for PIn and composites, and (d) PL spectra of GO, PIn and 15%GO/PIn composite.

Table 1 Optical bandgap energy of PIn, GO and GO/PIn nanocomposites

Material	Optical bandgap energy (E_g) (eV)
PIn	2.97
10%GO/PIn	2.66
15%GO/PIn	2.59
20%GO/PIn	2.80
25%GO/PIn	2.84
GO	2.62

inverse slope of the tangent using eqn (4). The E_u value calculated for PIn and composites is given in Table S2. The least value for E_u was obtained for 25%GO/PIn. The E_u values clearly demonstrated the high crystallinity of the nanocomposites compared to PIn.[24]

3.4. PL spectra

Laser-based PL spectra of GO, PIn and 15%GO/PIn composite were recorded to gain an insight into the phenomenon of migration, mobility extent and to determine the lifetime of the photogenerated electron–hole pairs.[26] The PL intensity was measured at an excitation wavelength of 325 nm in the range of 350–700 nm. The PL intensity gives information about the electron–hole recombination rate, where a high PL intensity corresponds to rapid electron–hole recombination. Fig. 3(d) represents the PL spectra in which the higher intensity peak was obtained for PIn at around 444 nm, attributed to n–π*and n–π*and polaronic transition in the PIn matrix, indicating the faster recombination rate.[48] The broad peak for GO was obtained at ~468 nm with a diminished intensity, which can be ascribed to a lower electron–hole recombination rate than that of PIn in the oxidized graphitic surface.[49] The 15%GO/PIn composite exhibited the lowest PL intensity, which can be attributed to the efficient charge transfer between the PIn matrix and the exfoliated GO layers. Hence, 15%GO/PIn seems to be a better photocatalyst as indicated by its UV-vis absorbance, band gap and PL spectrum, and can be considered as an optimized composition of GO and PIn for better photocatalytic activity.

3.5. Surface morphology

FESEM-EDAX was performed to investigate the surface characteristics of the synthesized materials, and is shown in Fig. 4. The FESEM images (Fig. 4(a) and (b)) obtained for PIn represent irregular shaped fused agglomerated particles with an average particle size of 150 nm.[50] Similar results were obtained by Phasuksom *et al.* for PIn synthesized by using $FeCl_3$ as an oxidant.[51] GO (Fig. 4(c)) exhibited a distorted surface with a stacked-sheet-like structure, confirming the exfoliation of the graphene sheets due to the oxidation of the graphitic layers.[34] Fig. 4(d) and (e) confirm the successful formation of the composite with PIn wrapped on the exfoliated GO sheets indicating a strong interaction between GO and PIn, giving rise to cauliflower-shaped morphology.[22] The EDAX data of 15%GO/PIn, as shown

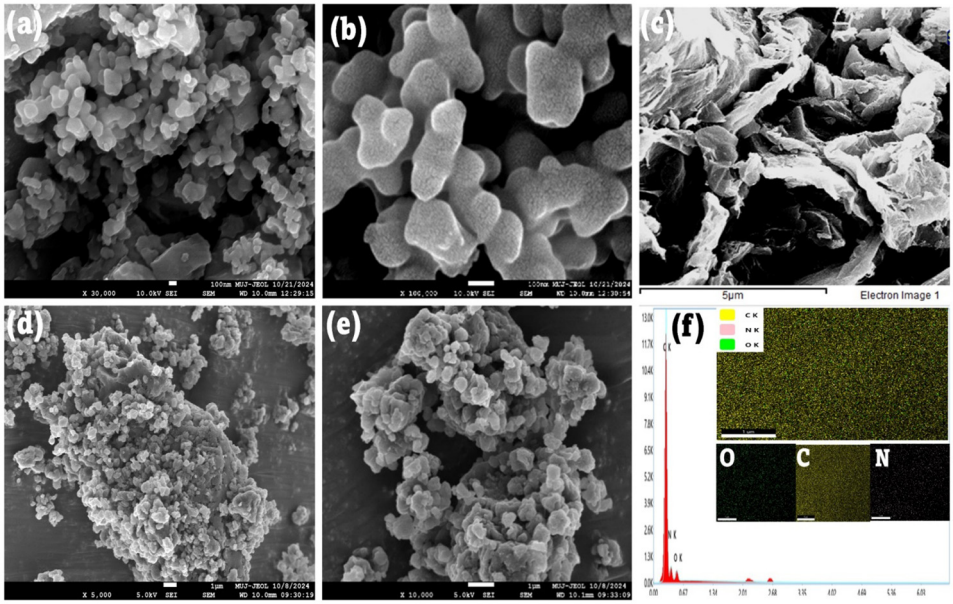

Fig. 4 FESEM images of (a) and (b) PIn, (c) GO and (d) and (e) 15%GO/PIn. (f) EDAX spectrum and color mapping of the 15%GO/PIn composite.

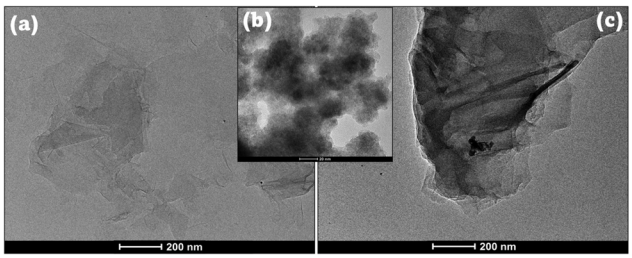

Fig. 5 TEM images of (a) GO, (b) PIn and (c) 15%GO/PIn composite.

in Fig. 4(f), verify the presence of characteristic elements, *i.e.* C, N and O, and their colored elemental mapping (Fig. S3) reveals the even distribution of elements in the microstructure.

To gain a deeper insight and compare the morphology of the pure materials with the composite, TEM was performed. The TEM image of GO (Fig. 5(a)) illustrates a (2D) highly transparent sheet-like structure, where the transparency was achieved due to a high degree of oxidation, leading to considerable exfoliation of GO sheets, as also reported by Sahil *et al.*[34] PIn being an amorphous polymeric material displayed small diffused structures (Fig. 5(b)). The colored elemental mapping patterns of PIn, GO, and 15%GO/PIn composite are given in Fig. S4–S6. The TEM image (Fig. 5(c)) of the 15%GO/PIn composite clearly displays a light grey sheet-like structure formed due to the homogenous decoration of darker polymeric PIn particles on transparent GO sheets. The TEM images provided an idea about the incorporation of PIn over GO sheets and the successful heterojunction formation.

3.6. XPS

XPS analysis was performed to gain insights into the elemental composition, oxidation state(s) and the chemical functionalities present in PIn, GO nanosheets and the hybrid cauliflower-shaped heterostructure.[26] Fig. 6(a) displays the survey spectra of the materials, which reveal the presence of C, O and N with the C 1s, N 1s and O 1s peak present at 285, 400 and 530 eV, respectively.[24] In the C 1s high-resolution spectra of PIn (Fig. 6(b)), the peaks at 284.1, 284.6 and 285.2 eV correspond to the sp^2, sp^3 and C–N bonds, respectively.[52] The N 1s spectra of PIn (Fig. 6(c)) reveal the presence of =N– at 398.2 eV, –NH– at 399.3 eV and $–NH^+$ states at 400.1 eV.[51,53,54] The peaks present at 530.55, 531.99 and 532.38 eV correspond to –O=C–OH, O=C and C–OH in the high-resolution O 1s spectra (Fig. 6(d)) of GO. The C 1s spectra of GO (Fig. 6(e)) represent three peaks centered at 284.2, 286.29 and 288.4 eV with C=C, C–C, C–O, C=O, and O–C=O bonds present at 284.20, 285.14, 286.29, 287.56 and 288.42 eV, respectively.[55] The 15%GO/PIn exhibited similar C 1s and N 1s spectra (Fig. 6(f) and (g)) as PIn with a slight shift in the C–N and $–NH^+$ peaks. This peak shifting towards a higher binding energy may be attributed to the change in morphology caused due to the origin of strong electrostatic interactions between GO and PIn following composite formation.[56] The extra peaks in N 1s (401.2 eV, N–C=O) and C 1s (286.7 eV, C–O) of 15%GO/PIn are due to the formation of new bonds between GO and PIn.[57] The O 1s spectra (Fig. 6(h)) of 15%GO/PIn show two peaks (C–O–C and O=C) similar to GO in addition to the appearance of a different peak present at 533.5 eV corresponding to –N–C=O, arising due to the formation of a new bond.[51] The XPS results explain the interactions resulting in peak shifting and new bond formations in GO/PIn composite that confirms the formation of the GO/PIn heterostructure.

3.7. BET and ZPC

N_2 adsorption–desorption isotherms were used to determine the textural properties of GO, PIn and 15%GO/PIn, and are presented in Fig. 7. The type IV isotherm was displayed by 15%GO/PIn, GO and PIn.[58] Table 2 presents the pore volume,

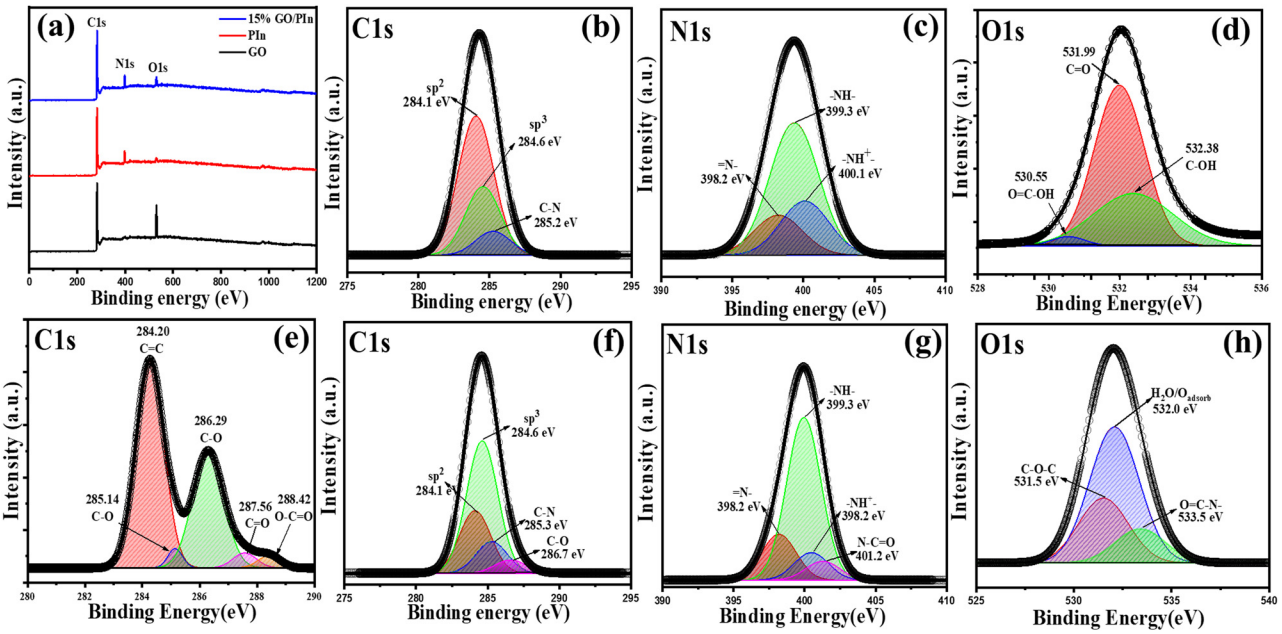

Fig. 6 XPS (a) survey spectra of GO, PIn and 15%GO/PIn. High-resolution spectra: (b) C 1s and (c) N 1s of PIn; (d) O 1s and (e) C 1s of GO; (f) C 1s, (g) N 1s and (h) O 1s of 15%GO/PIn.

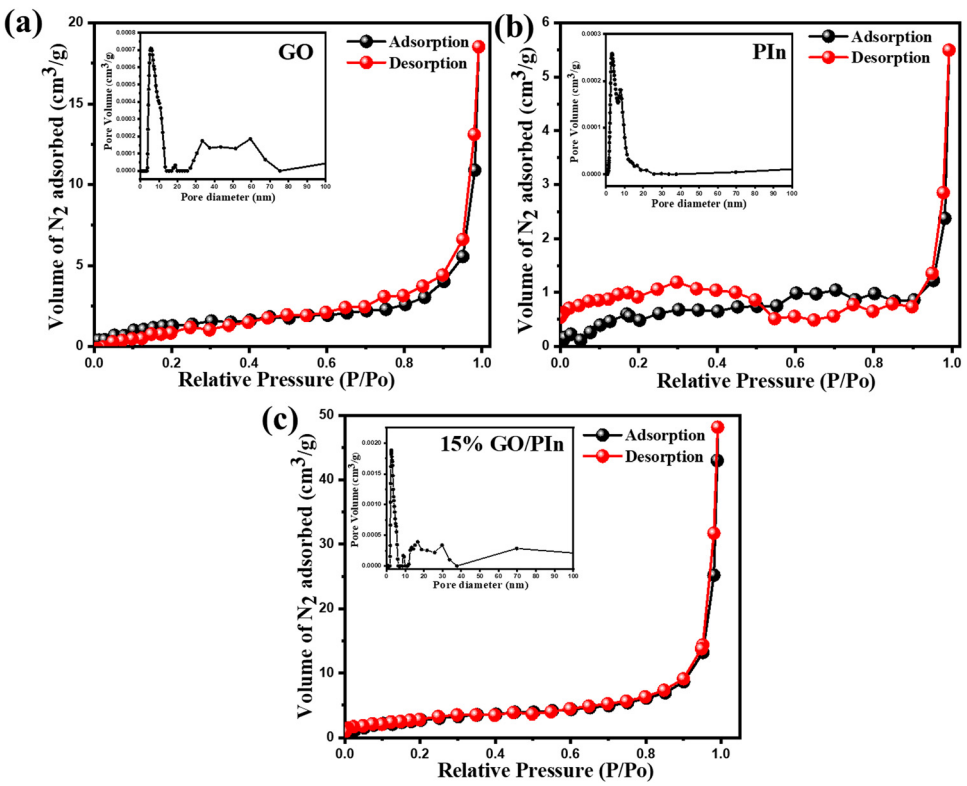

Fig. 7 N_2 adsorption–desorption isotherms of (a) GO, (b) PIn, and (c) 15%GO/PIn (insets: Barrett–Joyner–Halenda (BJH) pore size *vs.* pore volume distribution plots for the respective N_2 sorption isotherms).

pore size and specific surface area of all the materials. Notably, the surface area of the 15%GO/PIn composite was significantly increased due to the incorporation of PIn between the GO layers, resulting in exfoliation and consequently a larger surface area, which was also confirmed by the PXRD pattern. The 15%GO/PIn composite also possesses a higher pore size (nm) and pore volume ($cm^3\ g^{-1}$) than those of the constituent materials.

Table 2 BET textural results

Materials	Surface area (m^2 g^{-1})	Pore size (nm)	Pore volume (cm^3 g^{-1})
PIn	1.36	7.31	0.028
GO	5.51	15.23	0.004
15%GO/PIn	11.97	25.61	0.065

A zeta potential study was conducted to determine the zeta potential (mV) of 15%GO/PIn, and is given in Fig. S7. The surface of the material was found to be negatively charged with a zeta potential value of −21.3 mV. Singha *et al.* also obtained comparable results on modifying positively charged PIn with the negatively charged mercaptoacetate (MAA).[26] In a similar manner, it can be inferred in our study that the surface of PIn was probably positively charged, while GO was negatively charged due to the presence of oxygen-containing functional groups, as indicated in various studies reported in the literature.[34,59] Oppositely charged surfaces of the constituent materials with a difference in the ZPC values led to the formation of strong electrostatic interactions between GO and PIn.

3.8. Photoelectrochemical activity

Linear sweep voltammetry (LSV) measurements were performed both in the dark and under illumination to investigate the photoelectrocatalytic properties of the synthesized photocatalysts (GO, PIn, 15%GO/PIn) under visible light. The potential values referenced to Ag/AgCl were converted to the reversible hydrogen electrode (RHE) scale using the Nernst equation (eqn (5)):[60]

$$E(\mathrm{RHE}) = E(\mathrm{Ag/AgCl}) + 0.197 + 0.059\mathrm{pH} \quad (5)$$

Fig. 8(a) presents the current density *versus* potential curves for pristine GO, PIn and 15%GO/PIn photoanodes under both dark and illuminated conditions, as obtained through LSV measurements. The PEC analysis was performed using a three-electrode configuration, and the polarization curves revealed an anodic photocurrent response. Bare GO photoanode showed an increase in current density with the increase in voltage, suggesting its semiconductor behaviour.[61] It has a current density of 0.30 mA cm^{-2} at 1.8 V *vs.* RHE, which increases to 0.42 mA cm^{-2} upon illumination, attributed to enhanced photo-generation, leading to a large population of electron–hole pairs. The interaction between the graphene matrix and oxygen functional groups facilitates charge carrier excitation, where plasmons contribute to electron–hole pair formation by interacting with optical phonons at the edges of the graphene structure.[61] Similarly, PIn displays a current density of 0.24 mA cm^{-2} in the dark and 0.33 mA cm^{-2} under illumination at 1.8 V *vs.* RHE (Fig. 8(a) and Table S3). The binary composites exhibited higher current density values (Fig. S8), compared to the bare PIn and GO. The 15%GO/PIn composite showed maximum current density among all the composites, indicating a significant improvement in photoelectrocatalytic activity. A higher loading of GO leads to a decrease in activity, which might be due to the excessive agglomeration of PIn nanoparticles over GO sheets.[62] At 1.8 V *vs.* RHE, the

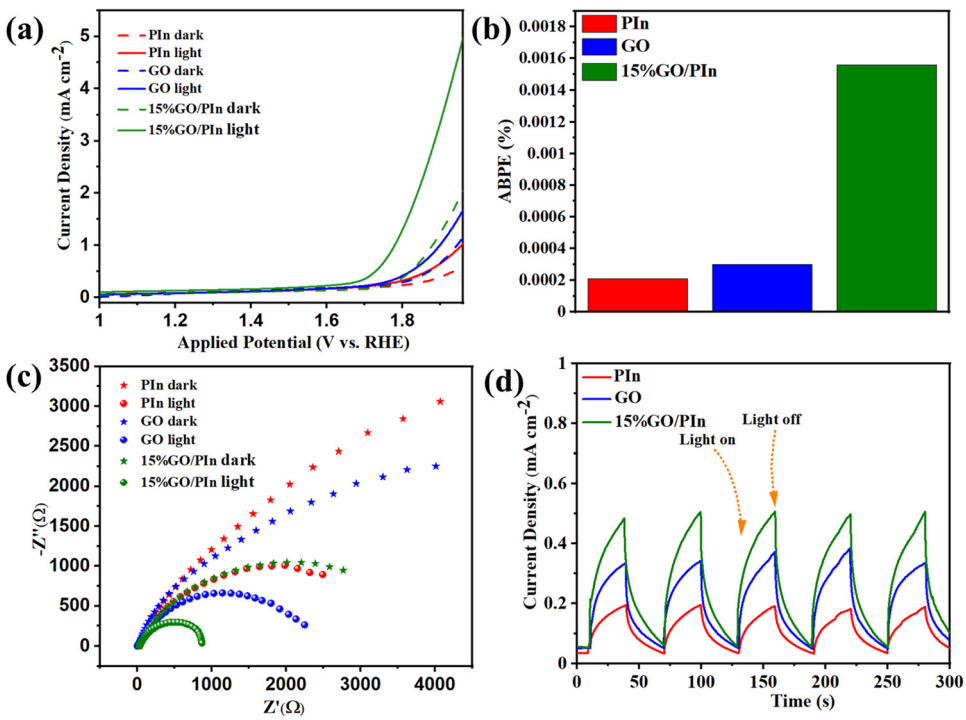

Fig. 8 (a) Polarisation curves obtained from linear sweep voltammetry measurements. (b) Bar diagram representing an applied bias photon-to-current efficiency of 1.2 V *vs.* RHE. (c) Nyquist plot obtained from electrochemical impedance spectroscopy measurements. (d) Transient photocurrent response in the dark and under illumination at 1.6 V *vs.* RHE.

15%GO/PIn composite achieves current densities of 0.39 mA cm^{-2} in the dark and 1.32 mA cm^{-2} under illumination. This enhancement can be attributed to improved charge separation and reduced electron–hole recombination, facilitated by the band alignment and synergistic interactions between the electronic structures of the components. The 15%GO/PIn heterojunction enabled an efficient visible light absorption by both components and reduced recombination by enhancing the charge transfer across the interface.

The applied bias photon-to-current efficiency (ABPE) (Fig. S9) for all the catalysts was determined from the LSV measurements at 1.2 V *vs.* RHE using the following equation:[63]

$$\mathrm{ABPE} = \frac{J(\mathrm{mA\ cm^{-2}})\left(1.23V - \left|V_{\mathrm{app}}\right|(V)\right)}{P_{\mathrm{light}}(\mathrm{mW\ cm^{-2}})} \times 100 \qquad (6)$$

where $|V_{app}|$ represents the applied bias at which the photocurrent density, "*J*", was measured, while 1.23 V *vs.* RHE corresponds to the thermodynamic potential for water splitting. The power density of the Xe arc lamp used for illumination is denoted as P_{light} (100 mW cm^{-2}). The ABPE values are presented in Fig. 8(b) and summarized in Table S3, with bar diagrams comparing the performance of the synthesized catalysts. The 15%GO/PIn composite demonstrated approximately 2.3-fold and 1.6-fold increases in photon-to-current efficiency compared to pure PIn and GO, respectively, highlighting the superior performance of the composite. This improvement in ABPE is consistent with the trends observed in the LSV measurements.

The intrinsic properties of materials can affect the interfacial characteristics of an electrochemical system. To assess these effects, ElS studies were conducted to obtain information on the charge transfer kinetics at the electrode/electrolyte interface of the various designed photocatalysts.[64] EIS studies were conducted at 1.6 V *vs.* RHE over a frequency range of 0.1 Hz to 10^5 Hz using an AC voltage. Impedance spectra contain a semicircular portion and the diameter of this semicircle represents charge transfer resistance (R_{ct}), as shown in Fig. 8(c). As compared to bare GO and PIn, the R_{ct} values for the GO/PIn composites are decreased, leading to a more efficient charge separation, confirming the acceleration in charge transfer ability following the composite formation. The 15%GO/PIn composite showed the least diameter of this semicircle, which decreased further upon light illumination. These results were found to be in order with the findings of the LSV measurements. The Bode phase plot (Fig. S10) further supports these observations with a shift of phase angle peak maxima to lower frequencies, suggesting an increase in the lifetime of the photogenerated charge carriers.[65] The 15%GO/PIn composite exhibits the longest charge carrier lifetime, as indicated by its peak maxima occurring at the lowest frequency. This enhancement is attributed to the synergistic interactions, which facilitate rapid charge transport, and the optimized band alignment between GO and PIn improving the charge separation efficiency.

The transient photocurrent response (Fig. 8(d)) was systematically evaluated to determine the photoresponsivity and photostability of the photocatalysts, both of which were crucial for assessing its long-term operational viability.[66] The chronoamperometric on/off cycles were performed over six intervals at an applied potential of 1.6 V *vs.* RHE, with alternating 30-second illumination and dark periods. The results align well with the trends observed in LSV measurements, showing a stable current density under dark conditions, followed by a significant enhancement upon illumination. The rapid decline in current density when the light source was switched off highlights the efficient photoresponse of the material as well as its stability during repeated cycles. The sustained and reproducible photocurrent response of 15%GO/PIn composite demonstrates its robustness for visible-light-driven photoelectrocatalysis, with negligible performance degradation over multiple on/off cycles. Furthermore, the transient photocurrent response of the 15%GO/PIn composite was compared with its individual components and the results revealed that it exhibited markedly higher responsivity and efficiency. This enhanced photoactivity is attributed to the strong interfacial charge transfer kinetics within the composite, which significantly improve charge transport and overall performance.

3.9. Photocatalytic evaluation

The photocatalytic efficiency of the synthesized photocatalysts was evaluated under visible light irradiation. To determine the best percentage composition among the synthesized composites, GO and PIn for the photodegradation reactions, a preliminary test was conducted on AO and EY. The 15%GO/PIn composite had shown the best photodegradation results with 74% and 85% degradation in 120 min for AO and EY, respectively. The percentage degradation trend for both the dyes was found to be PIn < 25%GO/PIn < 20% GO/PIn < GO < 10%GO/PIn < 15%GO/PIn, as demonstrated in Fig. 9(a) and (b). Further, a set of photodegradation reactions were conducted using the 15%GO/PIn composite for the fifteen different dyes, namely, AO, EY, VB, FB, AR, BB, Au, CBBR, BCG, CR, MV, MB, RhB, TB and CV. The percentage degradation values are listed in Table S4, and the respective UV absorbance spectra for all the dyes are presented in Fig. S11.

In order to examine the practical applications of the synthesized composite, further photocatalytic studies were conducted on the dye mixtures. The contaminated wastewater from different industries contains a mixture of different polluting chemical substances. For real practical application of wastewater treatment and real wastewater conditions, different dye mixtures were prepared and the reaction parameters were optimized to achieve the maximum photocatalytic efficiency. There are limited research reported in the literature on the degradation reactions of dye mixtures, and this concept remains largely unexplored. For example, Gupta *et al.* investigated the photocatalytic degradation of a dye mixture containing three dyes under sunlight using polymethyl methacrylate (PMMA)-based Ag/ZnO/TiO_2 nanofibers. In the dye mixtures, degradation rates of 81%, 66%, and 74.4% were achieved for different dyes, *i.e.* MB, Au, and FB, respectively.[67]

In the present study, anionic and cationic dye mixtures were separately prepared by taking four dyes for each mixture

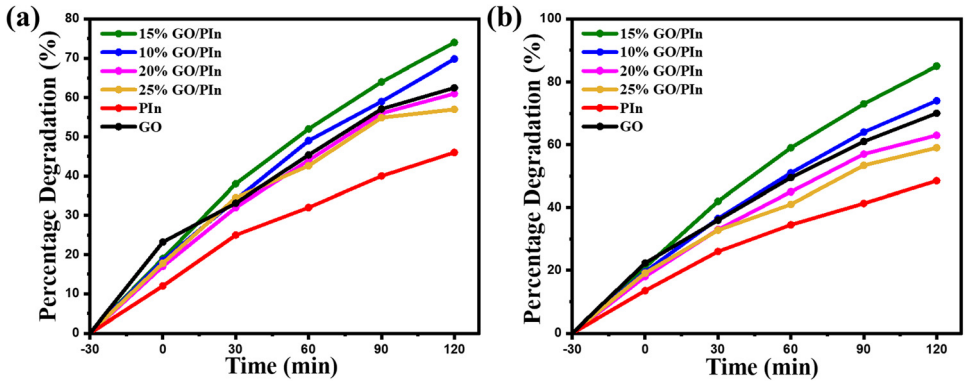

Fig. 9 Photocatalytic degradation graphs of (a) AO and (b) EY dye using GO, PIn and GO/PIn nanocomposites.

solution. The anionic dye mixture contains AR, EY, CBBR and BCG, whereas the cationic dye mixture consists of AO, BB, FB and VB. The various dyes present in the mixture are very different in their chemical structure, and each dye affects the biota in a different manner. The different photoreaction parameters (Fig. S12) such as catalyst dosage, initial dye concentration and pH were optimized for both anionic and cationic dye mixtures. The optimized catalyst dosage and initial dye concentration for both the anionic and cationic dye mixtures were determined to be 0.375 g L^{-1} and 10 ppm, respectively, while the pH was optimized to 10 for the cationic dye mixture and 4 for the anionic dye mixture to achieve the most effective photocatalytic degradation.

After optimizing all the photoreaction parameters, a final reaction was setup for 300 min under optimized conditions for both the dye mixtures. The photocatalytic degradation obtained for the anionic mixture was 84%, 78%, 83% and 70% for EY, AR, BCG and CBBR, respectively, and is shown in Fig. 10(a). For the cationic mixture, the photocatalytic degradation was found to be 87%, 82%, 81% and 85% for FB, BB, AO and VB, respectively, as shown in Fig. 10(b). The Ct/Co *vs.* time graphs for all the eight dyes in the mixtures in the absence of catalyst and in the presence of GO, PIn and 15%GO/PIn are given in Fig. S13.

A mixture with random concentrations of both anionic and cationic dyes was prepared to investigate the photocatalytic activity of the composite for an unregulated system (Fig. 10(c) and (d)). When all the dyes were taken at random concentrations, the peaks were not clearly distinguished and the phenomenon of peak merging was observed. In the random mixture, EY exhibited

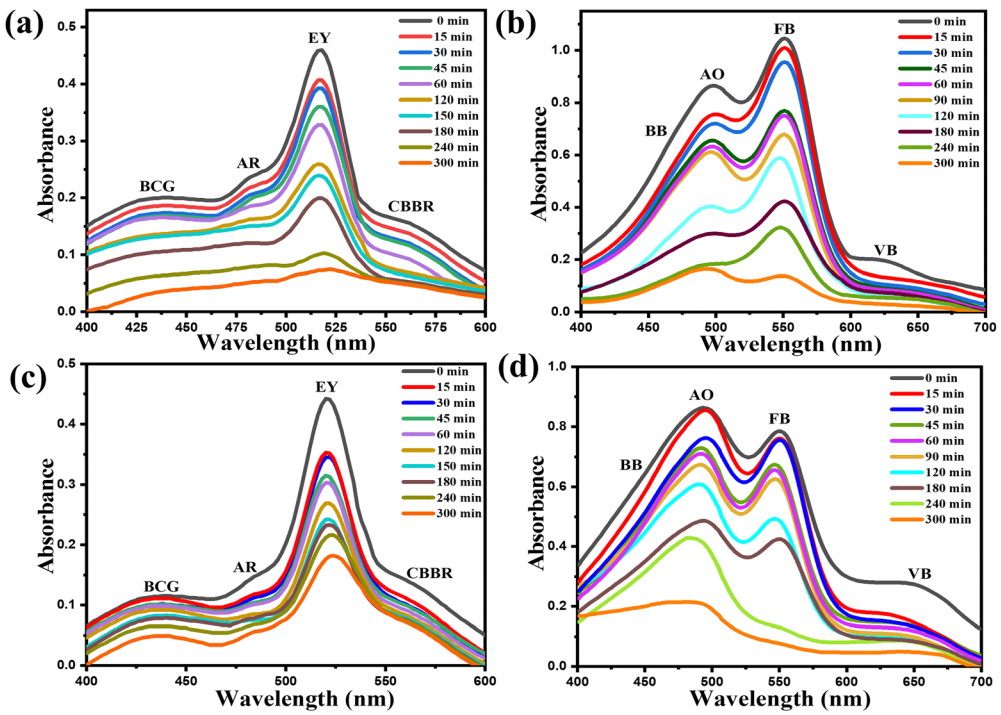

Fig. 10 UV-vis absorbance spectra of the photocatalytic degradation of (a) anionic mixture (10 ppm), (b) cationic mixture (10 ppm), (c) anionic mixture (random) and (d) cationic mixture (random).

the highest photocatalytic degradation in the anionic mixture, while FB in the cationic mixture. If the degradation is to be compared between the dyes present in anionic and cationic dye mixtures, the cationic mixture dyes showed higher degradation efficiencies. This can be attributed to the negatively charged surface of the 15%GO/PIn composite, which is confirmed by the ZPC analysis. The negatively charged catalyst surface proved to be an advantage for the adsorption of cationic dyes. Similar results were obtained by the Ribas *et al.*, where the oppositely charged surface of the catalyst and the dyes enhanced the adsorption and then photocatalysis.[68]

3.10. Kinetics of the photodegradation reaction:

The Langmuir–Hinshelwood (L–H) model was used to study the kinetics of the photo-degradation reaction by the 15%GO/PIn composite.[69] The equations used for pseudo-first- and second-order kinetics are as follows:

$$\ln C_0/C_t = K_1 t \quad (7)$$

$$1/C_t - 1/C_0 = K_2 t \quad (8)$$

For the pseudo-first-order kinetics, the plot between $\ln(C_0/C_t)$ and time shows a linear relationship, where the rate constant (k) can be determined by analyzing the slope. Similarly, the second-order-rate constant was determined from the slope of the plot between $1/C_t - 1/C_0$ and time.[34] The kinetic studies were conducted separately on all the eight dyes present in the anionic and cationic mixtures. The coefficient of determination (R^2) values for both pseudo-first- and pseudo-second-order kinetics are listed in Table 3. It can be concluded from the R^2 values listed in the table that the composite followed the pseudo-first-order kinetics for all cationic as well as anionic dyes. The pseudo-first-order rate constant values obtained for all the eight dyes lie in the range of 0.01–0.004 min^{-1}. The kinetic study graphs for pseudo-first- and second-order kinetics by 15%GO/PIn are given in Fig. 11.

Table 3 First- and second-order R^2 values and first-order rate constants for various dye photodegradation reactions

Dyes	Pseudo first order (R^2)	Pseudo second order (R^2)	Pseudo first order rate constant (K) min^{-1}
AR	0.87	0.87	0.010
EY	0.97	0.89	0.006
CBBR	0.85	0.81	0.004
BCG	0.94	0.81	0.005
AO	0.97	0.94	0.005
FB	0.95	0.78	0.006
BB	0.97	0.93	0.005
VB	0.87	0.85	0.004

3.11. Plausible mechanism for the photodegradation reaction

Based on the results obtained from the different characterizations and the photocatalytic experiments, the mechanism for the degradation of dyes using the 15%GO/PIn composite under visible light irradiation was elucidated. In brief, the incorporation of PIn within GO layers leads to the exfoliation of GO sheets, which increases its visible light absorption capacity

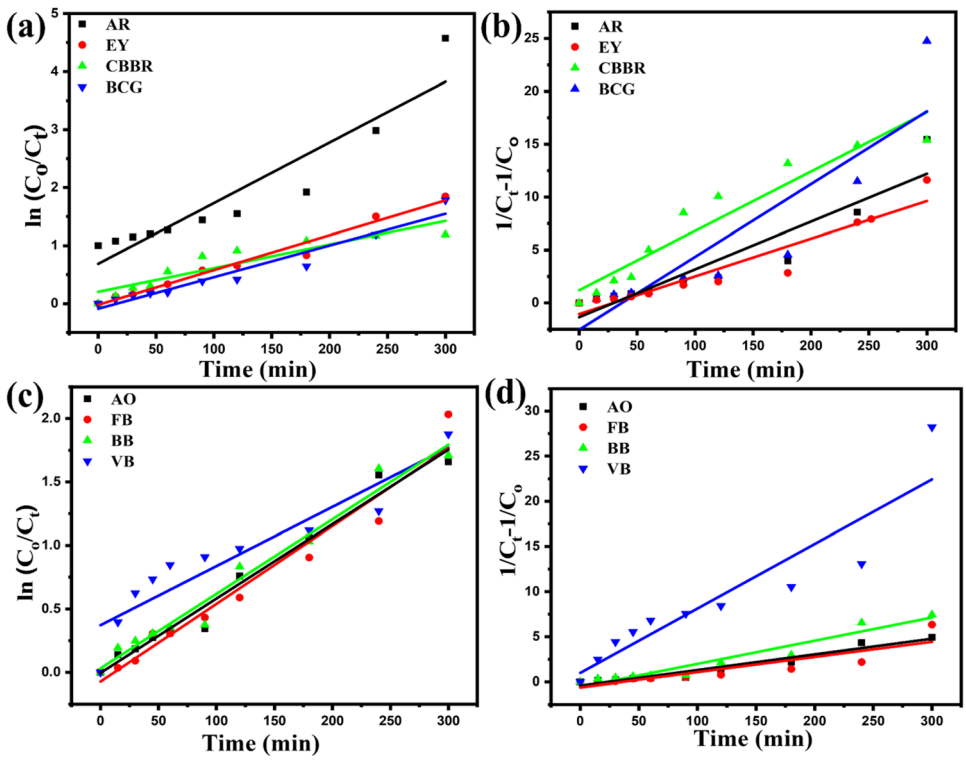

Fig. 11 (a) First-order and (b) second-order kinetics of the anionic mixture. (c) First-order (d) second-order kinetics of the cationic mixture.

resulting in an increase in the charge transfer, photocurrent density and photostability as evident from photocurrent response and EIS analyses. Moreover, upon formation of the heterojunction, the entire system establishes an appropriate band alignment between the components to significantly contribute to the improvement of photogenerated transfer of charge carriers when exposed to visible light. The Mott–Schottky measurements were conducted on the pristine materials to determine their flat band potential (E_{FB}) and infer the photocatalytic degradation mechanism and is given in Fig. 12(a) and (b). The negative slopes obtained for both GO and PIn suggested their p-type semiconductor behavior with their E_{FB} approximately equal to the valence band potential (E_{VB}). The E_{FB} values obtained for PIn and GO were 1.12 and 1.53 V *vs.* Ag/AgCl, respectively. For p-type semiconductors, the value of E_{VB} is generally +0.3 V from their respective E_{FB}.[70] The combined results obtained from the UV-visible spectra (Tauc plots) and MS plots provided the VB and CB edge potentials for GO to be +2.04 and −0.58 V *vs.* NHE, respectively. The VB and CB edge potentials of PIn were calculated to be +1.63 and −1.34 V *vs.* NHE, respectively. The relative alignment of the CB and VB in GO and PIn supports a Z-scheme charge transfer mechanism governing the degradation process.

Therefore, to gain a deeper understanding of the mechanism, scavenger experiments were conducted to determine the generation of $^{\bullet}OH$ and $^{\bullet}O_2^-$ radicals within the 15%GO/PIn composite. IPA, EDTA, and BQ were used as the scavengers for $^{\bullet}OH$, h^+, and $^{\bullet}O_2^-$, respectively. Fig. 12(c) and (d) clearly depict that the BQ addition significantly reduced the photocatalytic degradation of dyes, while EDTA and IPA showed a slight decrease. As a result of this experiment, the order of ROS participation in photocatalytic dye degradation was deduced as ($^{\bullet}O_2^-$) > ($^{\bullet}OH$) > (h^+), making $^{\bullet}O_2^-$ as the primary radical species followed by $^{\bullet}OH$ and h^+. To confirm the generation of these ROS, ESR experiments were conducted using 5,5-dimethyl-1-pyrroline-*N*-oxide (DMPO) as the spin trapping agent. As shown in Fig. 12(e) and (f), no signals were detected for $^{\bullet}OH$ and $^{\bullet}O_2^-$ under dark conditions. After the irradiation of visible light for 10 min, four distinct peaks with 1 : 2 : 2 : 1 intensity were obtained for DMPO–$^{\bullet}OH$ whereas DMPO–$^{\bullet}O_2^-$ exhibited six peaks but with no trend in the intensities. $^{\bullet}OH$ generated in the aqueous medium forms DMPO–$^{\bullet}OH$ and $^{\bullet}O_2^-$ in methanol forms DMPO–$^{\bullet}O_2^-$ adducts, confirming the existence of $^{\bullet}OH$ and $^{\bullet}O_2^-$ radicals.[71] This demonstrates that the $^{\bullet}O_2^-$ and $^{\bullet}OH$ radicals were generated and played a significant role in the photocatalytic degradation of dyes.

The possible charge transfer pathway in the 15%GO/PIn composite for dye degradation follows the Z-scheme transfer (Fig. 13), and is given below:

$$\text{GO/PIn} + h\nu\ (\text{Vis}) \rightarrow \text{GO/PIn}^*\ (h^+ + e^-)$$

$$\text{GO} + h\nu\ (\text{Vis}) \rightarrow \text{GO}^*\ (h^+\ \text{VB} + e^-\ \text{CB}).$$

$$\text{PIn} + h\nu\ (\text{Vis}) \rightarrow \text{PIn}^*\ (h^+\ \text{HOMO} + e^-\ \text{LUMO})$$

$$\text{GO}^*\ (e^-\ \text{CB}) \rightarrow \text{PIn}^*\ (e^-\ \text{HOMO})\ \{e^-\ \text{transfer}\}$$

$$\text{PIn}^*\ (e^-\ \text{HOMO}) \rightarrow \text{PIn}^*(e^-\ \text{LUMO})\ \{e^-\ \text{transfer}\}$$

$$\text{GO}^*\ (h^+\ \text{VB}) + H_2O \rightarrow {}^{\bullet}OH\ (\text{active species})$$

$$\text{PIn}^*\ (e^-\ \text{LUMO}) + O_2 \rightarrow {}^{\bullet}O_2^-\ (\text{active species})$$

$$^{\bullet}O_2^- + 2\ H^+ \rightarrow H_2O_2$$

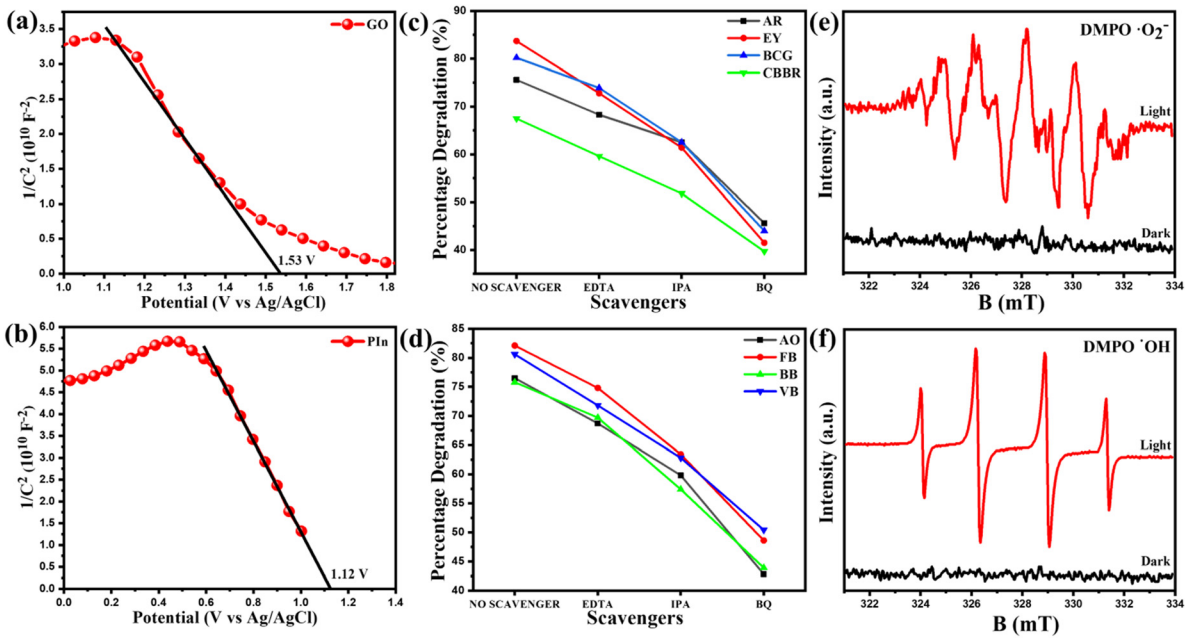

Fig. 12 Mott–Schottky plots of (a) GO and (b) PIn. Scavenger studies of (c) anionic and (d) cationic dyes. ESR spectra of (e) DMPO–$^{\bullet}O_2^-$ and (f) DMPO–$^{\bullet}OH$.

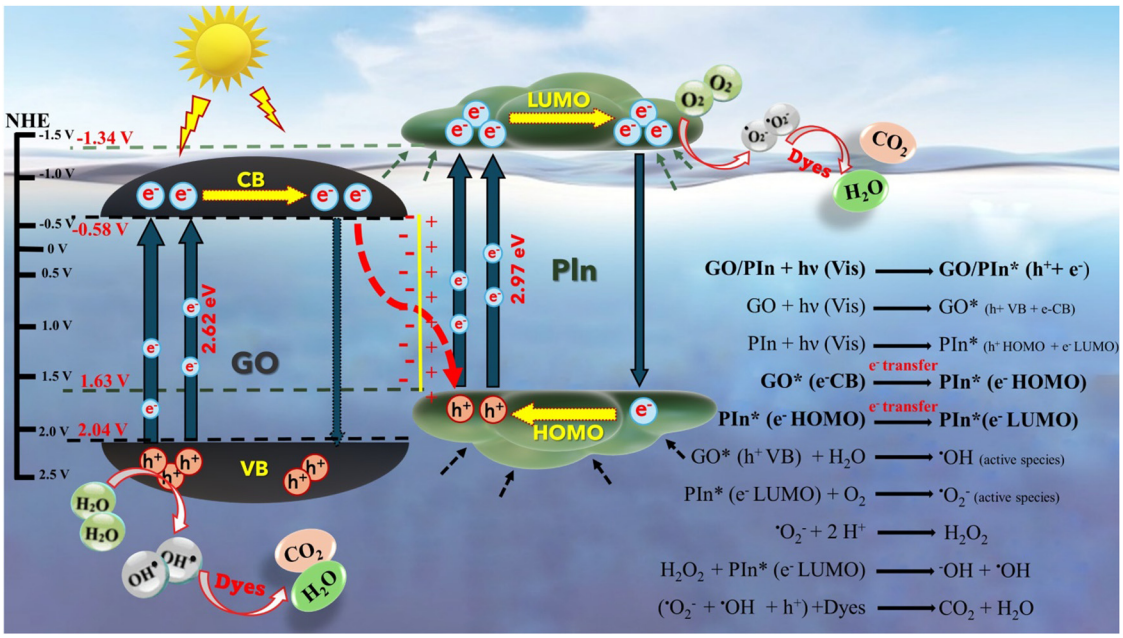

Fig. 13 Plausible photocatalytic mechanism of dye degradation by the GO/PIn composite: diagrammatic representation and proposed pathway scheme.

$$H_2O_2 + PIn^* (e^- \text{ LUMO}) \rightarrow {}^-OH + {}^\bullet OH$$

$$({}^\bullet O_2{}^- + {}^\bullet OH + h^+) + \text{Dyes} \rightarrow CO_2 + H_2O$$

When the surface of the composite gets irradiated by the visible light, the photons transfer their energy to e^-s present in the VB, which excites them to the CB, creating vacant positions in the VB called holes. The phenomenon of photo-induced charge separation occurs in both GO and PIn, simultaneously. The photoexcited e^-s in CB of GO are readily transferred to the HOMO of PIn due to the presence of an internal electric field (IEF) at the heterojunction interface.[72] This electron migration initiates the Z-scheme charge transfer pathway, thereby facilitating the effective separation and transport of photogenerated charge carriers during the photocatalytic process. These e^-s from the HOMO of PIn further get excited to the LUMO. Thus, the separated charge densities at the two extreme ends of the 15%GO/PIn composite initiate the generation of $^\bullet OH$ and $^\bullet O_2{}^-$. The photoexcited electrons that were accumulated in the LUMO of the PIn possess adequate thermodynamic potential of −1.34 V *vs.* NHE to reduce dissolved O_2 into superoxide radicals ($^\bullet O_2{}^-$) (−0.33 V *vs.* NHE), and the photogenerated holes that were present uninterrupted in the VB of GO have the potential (+2.04 V *vs.* NHE) in the close vicinity of the required standard potential (1.99 V *vs.* NHE for $OH^-/^\bullet OH$ and 2.27 V *vs.* NHE for $H_2O/^\bullet OH$) for $^\bullet OH$ generation. For the 15%GO/PIn composite, enhanced photocatalytic performance can be ascribed to the formation of interface between GO and PIn, enabling Z-scheme charge transfer dynamics. This configuration effectively promotes the separation of photoinduced electron–hole (e^-/h^+) pairs, confirmed by the PL and Nyquist plots. These ROS further reacts with the dyes adsorbed on the surface of the catalyst and gets readily oxidized to give simple non-harmful products. For example, the degradation pathway of the FB dye occurs through a sequence of chemical reactions involving steps such as hydroxylation, ring-opening, and oxidation, where it is ultimately converted into simpler inorganic compounds such as water (H_2O) and carbon dioxide (CO_2). Similar products of the FB dye were obtained by Sharma *et al.*[73] and Wang *et al.*,[74] where the intermediates and the final products were confirmed by employing mass spectrometry. The degradation pathway of the FB dye proposed by Wang *et al.* involves the initial electrophilic addition of hydroxyl radicals ($^\bullet OH$) to the dye molecule, followed by successive oxidation steps that result in the cleavage of the central carbon–carbon double bond. This process generates various intermediate compounds such as 1,4 cyclohexanedione, 4-aminobenzaldehyde and *p*-benzoquinone, which subsequently undergo further oxidation and mineralization into CO_2 and H_2O.

3.12. Recyclability

The recyclability of the 15%GO/PIn as a photocatalyst was determined by employing it to the eight photocatalytic degradation cycles for the FB dye. The reaction conditions for each cycle were kept the same and the catalyst was washed with ethanol and double-distilled water to remove the adsorbed dye molecules followed by drying after each cycle. It is to be noted that the composite was easily extractable from the dye solution due to the presence of hydrophobic PIn. As given in Fig. 14(a), 15%GO/PIn maintained a remarkable consistency for photocatalytic activity up to eight cycles with minimal decrease in efficiency. The slight decrease was attributed to the loss of the catalyst during extraction and washing. A comparative table (Table S5) is provided, summarizing the relative photocatalytic

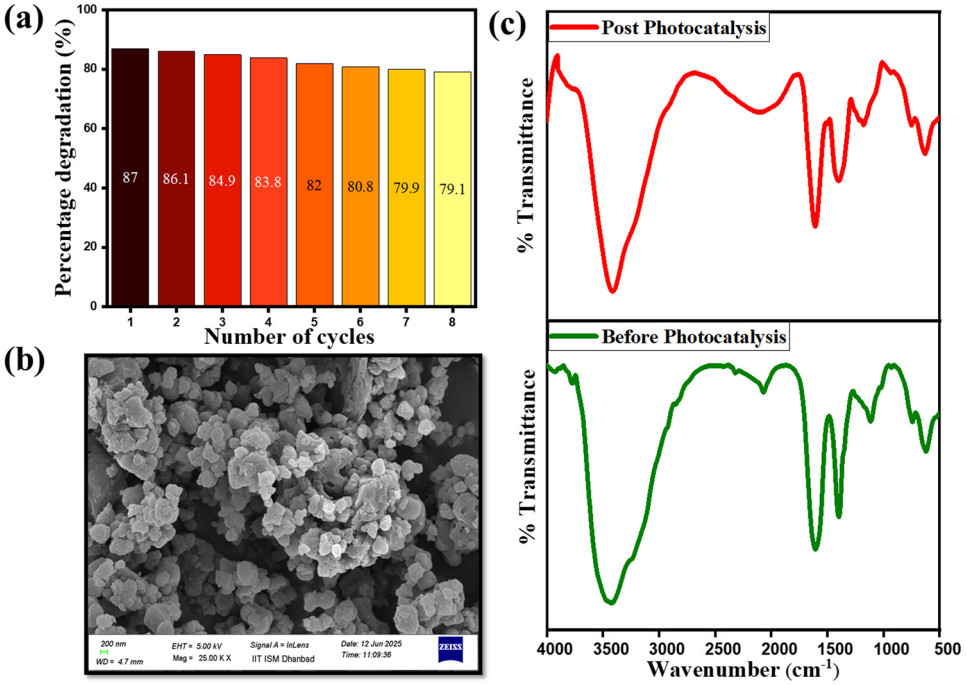

Fig. 14 (a) Recyclability studies of the 15%GO/PIn composite for FB dye degradation. Post-photocatalytic (b) FESEM image and (c) FTIR spectra of the 15%GO/PIn composite before and after eight cycles.

efficiency, recyclability, and post-cyclic efficiency of 15%GO/PIn with recently reported systems in the literature. Post-photocatalytic FESEM and FTIR spectroscopy were performed to establish the structural stability of the 15%GO/PIn composite. There was no significant difference observed in the morphology (Fig. 14(b)) of the composite after eight photocatalytic cycles of FB dye degradation when compared to the fresh sample. Fig. 14(c) shows a comparison of the composite's FTIR spectra before and after eight cycles, with no remarkable differences in peak positions and intensity, indicating evidence of strong chemical stability. This demonstrated the outstanding structural stability of 15%GO/PIn throughout photocatalytic processes, proving it as an effective multicyclic photocatalyst suitable for use in a variety of applications.

4. Conclusion

A series of *x*%GO/PIn (*x*% = 10, 15, 20 and 25) composites have been successfully synthesized using an *in situ* chemical oxidative polymerization technique by varying the amount of GO in the PIn matrix. The GO/PIn composite was employed for the photocatalytic application and demonstrated excellent results in degrading dye mixtures under visible light irradiation. The photocatalytic activity of the composites was initially tested on AO and EY dyes, followed by the anionic and cationic dye mixtures separately. A mixture of dyes was taken to mimic the real wastewater conditions to test the practical applications of the synthesized composite. The structural, optical and morphological characteristics of GO, PIn and GO/PIn composites were successfully determined using XRD, FTIR Spectroscopy, XPS, BET, UV-vis Spectroscopy, PL and SEM-EDAX The photoelectrochemical properties of the materials were investigated by LSV, EIS and chronoamperometric on/off measurements. Among all the synthesized catalysts, 15%GO/PIn composite showed the best results in all the photocatalytic experiments. The synergistic effect between GO and PIn in the composite led to a significant increase in its visible light absorption capacity and low electron hole recombination rate, which were confirmed by the PL and EIS. The kinetic studies were conducted for the photodegradation reactions by 15%GO/PIn composite and found to follow the pseudo-first-order kinetics with high precision and higher rate constants compared to the pseudo-second-order kinetics. The plausible photocatalytic degradation mechanism was deduced where the active radical species were determined by employing the radical scavengers. The composite demonstrated high recyclic stability where it showed consistent degradation efficiency up to eight consecutive cycles. Hence, the GO/PIn composites proved to be efficient multicyclic photocatalysts, which can be employed for practical wastewater treatment. This article demonstrated the scope of employing the GO/PIn composite further in different domains such as electrocatalysis, photo-electrocatalysis for the environmental remediation and real-world applications.

Conflicts of interest

The authors have no conflicts of interest to declare.

Data availability

The data that support the findings of this study are available from the authors.

Literature table for dye mixtures; absorbance spectra and band gap calculation of 15%GO/PIn using UV-DRS; Urbach energy table for PIn and composites; FESEM image and colored elemental mapping of 15%GO/PIn; HAADF-STEM images and elemental mapping of GO, PIn and 15%GO/PIn; zeta potential data of 15%GO/PIn; LSV polarization curves and bar diagram representing applied bias photon-to-current efficiency at 1.2 V *vs.* RHE of the synthesized catalysts; comparison table for current densities; Bode phase plots; UV absorbance spectra and photodegradation values table for fifteen dyes using 15%GO/PIn; photoreaction parameter optimization graphs and explanation for dye mixtures; Ct/Co *vs.* time (min) graphs of eight mixture dyes; relative efficiency comparison table of 15%GO/PIn composite with recent reported literature. See DOI: **https://doi.org/10.1039/d5ma00429b**

Acknowledgements

The authors are thankful for the XPS facility at CRF, IIT(ISM) Dhanbad. The authors are also grateful to CRF, IIT Delhi for BET facility.

References

1 A. Hussain, R. Kumari, S. G. Sachan and A. Sachan, *Microbial Ecology of Wastewater Treatment Plants*, Elsevier, 2021, pp. 175–192.
2 J. Lin, W. Ye, M. Xie, D. H. Seo, J. Luo, Y. Wan and B. Van der Bruggen, *Nat. Rev. Earth Environ.*, 2023, **4**, 785–803.
3 R. Al-Tohamy, S. S. Ali, F. Li, K. M. Okasha, Y. A.-G. Mahmoud, T. Elsamahy, H. Jiao, Y. Fu and J. Sun, *Ecotoxicol. Environ. Saf.*, 2022, **231**, 113160.
4 R. Saravanathamizhan and V. T. Perarasu, *Wastewater Treatment*, Elsevier, 2021, pp. 103–136.
5 A. Ahmad, S. H. Mohd-Setapar, C. S. Chuong, A. Khatoon, W. A. Wani, R. Kumar and M. Rafatullah, *RSC Adv.*, 2015, **5**, 30801–30818.
6 H. Kumari, Sonia, Suman, R. Ranga, S. Chahal, S. Devi, S. Sharma, S. Kumar, P. Kumar, S. Kumar, A. Kumar and R. Parmar, *Water, Air, Soil Pollut.*, 2023, **234**, 349.
7 P. Pal, *Industrial Water Treatment Process Technology*, Elsevier, 2017, pp. 537–544.
8 S. Ali, J. Abdul Nasir, R. Nasir Dara and Z. Rehman, *Inorg. Chem. Commun.*, 2022, **145**, 110011.
9 H. He, *Solution Processed Metal Oxide Thin Films for Electronic Applications*, Elsevier, 2020, pp. 7–30.
10 Hisana, A. Shahzaib, N. Nishat, S. M. Alshehri, T. Ahamad and Z. Haque, *Hybrid Adv.*, 2024, **5**, 100145.
11 J. Prakash, S. Sun, H. C. Swart and R. K. Gupta, *Appl. Mater Today*, 2018, **11**, 82–135.
12 Samriti, Maneet, T. Ahuja and J. Prakash, *Gold and Silver Nanoparticles*, Elsevier, 2023, pp. 379–410.
13 J. Prakash and H. Swart, *Phys. B*, 2023, **669**, 415297.
14 I. Ali, A. A. Basheer, X. Y. Mbianda, A. Burakov, E. Galunin, I. Burakova, E. Mkrtchyan, A. Tkachev and V. Grachev, *Environ. Int.*, 2019, **127**, 160–180.
15 S. Thakur, A. Ojha, S. K. Kansal, N. K. Gupta, H. C. Swart, J. Cho, A. Kuznetsov, S. Sun and J. Prakash, *Adv. Powder Mater.*, 2024, **3**, 100233.
16 G. Wang, B. Wang, J. Park, J. Yang, X. Shen and J. Yao, *Carbon*, 2009, **47**, 68–72.
17 M. Ghorbani, H. Esfandian, N. Taghipour and R. Katal, *Desalination*, 2010, **263**, 279–284.
18 N. N. Hanafi, K. P. Sambasevam, A. Arifutzzaman, S. Rahman and S. N. A. Baharin, *Orbital: Electron. J. Chem.*, 2020, **12**, 205–212.
19 M. K. Gunawardana, H. N. Disanayaka, M. Shanika Fernando, K. M. N. de Silva and R. M. de Silva, *Results Chem.*, 2023, **6**, 101079.
20 N. S. Wadatkar and S. A. Waghuley, *Indian J. Phys.*, 2018, **92**, 1551–1559.
21 N. Mushahary, A. Sarkar, F. Basumatary, S. Brahma, B. Das and S. Basumatary, *Results Surf. Interfaces*, 2024, **15**, 100225.
22 K. Phasuksom, W. Prissanaroon-Ouajai and A. Sirivat, *RSC Adv.*, 2020, **10**, 15206–15220.
23 Q. Zhou, D. Zhu, X. Ma, J. Xu, W. Zhou and F. Zhao, *RSC Adv.*, 2016, **6**, 29840–29847.
24 R. Gopika, K. Arun and M. T. Ramesan, *Langmuir*, 2024, **40**, 8046–8058.
25 S. Megha, D. Devadathan, V. Baiju and R. Raveendran, *J. Phys.: Conf. Ser.*, 2019, **1172**, 012051.
26 K. Singha, G. Kumari, S. Jagadevan, A. N. Sarkar and S. Pal, *Langmuir*, 2024, **40**, 16208–16225.
27 Samriti, S. Thakur, A. Ojha, R. Gupta, M. Bechelany, A. Yu Kuznetsov, H. C. Swart and J. Prakash, *Phys. Status Solidi A*, 2024, 2400169.
28 D. C. Marcano, D. V. Kosynkin, J. M. Berlin, A. Sinitskii, Z. Sun, A. Slesarev, L. B. Alemany, W. Lu and J. M. Tour, *ACS Nano*, 2010, **4**, 4806–4814.
29 S. Stankovich, D. A. Dikin, R. D. Piner, K. A. Kohlhaas, A. Kleinhammes, Y. Jia, Y. Wu, S. T. Nguyen and R. S. Ruoff, *Carbon*, 2007, **45**, 1558–1565.
30 P. Chhattise, K. Handore, A. Horne, K. Mohite, A. Chaskar, S. Dallavalle and V. Chabukswar, *J. Chem. Sci.*, 2016, **128**, 467–475.
31 W.-K. Jang, J. Yun, H.-I. Kim and Y.-S. Lee, *Colloid Polym. Sci.*, 2013, **291**, 1095–1103.
32 W. Peng, H. Li, Y. Hu, Y. Liu and S. Song, *Mater. Res. Bull.*, 2016, **74**, 333–339.
33 H. Yu, B. Zhang, C. Bulin, R. Li and R. Xing, *Sci. Rep.*, 2016, **6**, 36143.
34 S. Thakur, A. Badoni, Samriti, P. Sharma, A. Ojha, H. C. Swart, A. Y. Kuznetsov and J. Prakash, *Langmuir*, 2024, **40**, 18486–18502.
35 M. Karegar and M. M. Khodaei, *Polym. Bull.*, 2022, **79**, 11431–11460.
36 H. Mudila, S. Rana, M. G. H. Zaidi and S. Alam, *Fullerenes, Nanotubes Carbon Nanostruct.*, 2015, **23**, 20–26.
37 K. Phasuksom, W. Prissanaroon-Ouajai and A. Sirivat, *RSC Adv.*, 2020, **10**, 15206–15220.
38 W. Zhou and J. Xu, *Polym. Rev.*, 2017, **57**, 248–275.

39 R. Mishra, N. R. Nirala, R. K. Pandey, R. P. Ojha and R. Prakash, *Langmuir*, 2017, **33**, 13572–13580.
40 V. Divya, Y. Jeetika and M. V. Sangaranarayanan, *Mater. Today Proc.*, 2020, **26**, 97–103.
41 C. J. Verma, A. S. Keshari, P. Dubey and R. Prakash, *Vacuum*, 2020, **177**, 109363.
42 D. Gogoi, P. Makkar and N. N. Ghosh, *ACS Omega*, 2021, **6**, 4831–4841.
43 H. Zengin and G. Kalaycı, *Mater. Chem. Phys.*, 2010, **120**, 46–53.
44 B. Begum, S. Ijaz, R. Khattak, R. A. Qazi, M. S. Khan and K. H. Mahmoud, *Polymers*, 2021, **14**, 3.
45 A. Nihmath and M. T. Ramesan, *J. Inorg. Organomet. Polym. Mater.*, 2017, **27**, 481–489.
46 Ö. B. Mergen and E. Arda, *Synth. Met.*, 2020, **269**, 116539.
47 F. Urbach, *Phys. Rev.*, 1953, **92**, 1324.
48 Y. Elkony, M. Ali, S. Ebrahim and R. Adel, *J. Inorg. Organomet. Polym. Mater.*, 2022, **32**, 3106–3116.
49 N. S. Das, K. K. Gogoi and A. Chowdhury, *Semicond. Sci. Technol.*, 2021, 465–471.
50 M. Elango, M. Deepa, R. Subramanian and A. Mohamed Musthafa, *Polym.-Plast. Technol. Eng.*, 2018, **57**, 1440–1451.
51 K. Phasuksom and A. Sirivat, *Synth. Met.*, 2016, **219**, 142–153.
52 R. P. Raj, P. Ragupathy and S. Mohan, *J. Mater. Chem. A*, 2015, **3**, 24338–24348.
53 L. Xu, D. Li, W. Zhou, Y. Ding, Y. Wu, J. Xu and X. Duan, *Arabian J. Chem.*, 2020, **13**, 6061–6071.
54 A. Thadathil, N. Edavan Chathoth, Y. A. Ismail, P. Anjukandi and P. Periyat, *J. Phys. Chem. C*, 2022, **126**, 16965–16982.
55 R. Al-Gaashani, A. Najjar, Y. Zakaria, S. Mansour and M. A. Atieh, *Ceram. Int.*, 2019, **45**, 14439–14448.
56 T. Li, J.-D. Cui, L.-M. Gao, Y.-Z. Lin, R. Li, H. Xie, Y. Zhang and K. Li, *ACS Sustainable Chem. Eng.*, 2020, **8**, 13352–13361.
57 L. Peng, J. Han, H. Zhang, L. Ren, J. Li and J. Chen, *Langmuir*, 2024, **40**, 19493–19505.
58 M. A. Al-Ghouti and D. A. Da'ana, *J. Hazard. Mater.*, 2020, **393**, 122383.
59 M. Li, C. Liu, Y. Xie, H. Cao, H. Zhao and Y. Zhang, *Carbon*, 2014, **66**, 302–311.
60 N. Garg and A. K. Ganguli, *RSC Adv.*, 2024, **14**, 26292–26301.
61 D. O. Idisi, C. C. Ahia, E. L. Meyer, J. O. Bodunrin and E. M. Benecha, *RSC Adv.*, 2023, **13**, 6038–6050.
62 J. Heo, H. Bae, P. Mane, V. Burungale, C. Seong and J.-S. Ha, *ACS Omega*, 2023, **8**, 32794–32803.
63 M. Shaban, M. Rabia, A. M. A. El-Sayed, A. Ahmed and S. Sayed, *Sci. Rep.*, 2017, **7**, 14100.
64 K. Surana, R. M. Mehra, S. S. Soni and B. Bhattacharya, *RSC Adv.*, 2022, **12**, 1352–1360.
65 P. Shinde, A. Punde, S. Shah, A. Waghmare, Y. Hase, B. Bade, V. Doiphode, S. Ladhane, S. Rahane, D. Kale, S. Rondiya, M. Prasad and S. Jadkar, *Int. J. Hydrogen Energy*, 2024, **54**, 1073–1084.
66 K. Li, Z. Huang, X. Zeng, B. Huang, S. Gao and J. Lu, *ACS Appl. Mater. Interfaces*, 2017, **9**, 11577–11586.
67 A. Gupta, N. Khosla, V. Govindasamy, A. Saini, K. Annapurna and S. R. Dhakate, *Appl. Nanosci.*, 2020, **10**, 4191–4205.
68 L. Nascimento Ribas, L. O. de Sousa Bulhões and W. L. da Silva, *Water, Air, Soil Pollut.*, 2020, **231**, 191.
69 A. Farhan, M. Zahid, N. Tahir, A. Mansha, M. Yaseen, G. Mustafa, M. A. Alamir, I. M. Alarifi and I. Shahid, *Sci. Rep.*, 2023, **13**, 9497.
70 V. L. E. Siong, X. H. Tai, K. M. Lee, J. C. Juan and C. W. Lai, *RSC Adv.*, 2020, **10**, 37905–37915.
71 X. Li, B. Wang, W. Yin, J. Di, J. Xia, W. Zhu and H. Li, *Acta Phys.-Chim. Sin.*, 2020, **36**, 4308–4319.
72 K. Boukayouht, N. U. M. Nor, Y. Ait-Khouia, W. L. Queen, N. A. Saidina Amin and S. El Hankari, *Inorg. Chem.*, 2025, **64**, 4308–4319.
73 R. Sharma, B. Pal and S. Barman, *Environ. Sci. Pollut. Res.*, 2024, **31**, 66248–66261.
74 S. Wang, D. Li, C. Sun, S. Yang, Y. Guan and H. He, *J. Mol. Catal. A: Chem.*, 2014, **383–384**, 128–136.